A&A 594, A1 (2016)
DOI: 10.1051/0004-6361/201527101

Astronomy & Astrophysics
Special feature

Planck 2015 results

Planck 2015 results

I. Overview of products and scientific results

Planck Collaboration: R. Adam[105], P. A. R. Ade[126], N. Aghanim[84], Y. Akrami[89,148], M. I. R. Alves[143,14,84], F. Argüeso[28], M. Arnaud[103], F. Arroja[94,109], M. Ashdown[98,9], J. Aumont[84], C. Baccigalupi[123], M. Ballardini[46,70,72], A. J. Banday[143,14], R. B. Barreiro[92], J. G. Bartlett[1,95], N. Bartolo[45,94], S. Basak[123], P. Battaglia[48,50], E. Battaner[146,147], R. Battye[96], K. Benabed[85,140], A. Benoît[82], A. Benoit-Lévy[35,85,140], J.-P. Bernard[143,14], M. Bersanelli[49,71], B. Bertincourt[84], P. Bielewicz[116,14,123], I. Bikmaev[30,4], J. J. Bock[95,16], H. Böhringer[111], A. Bonaldi[96], L. Bonavera[26], J. R. Bond[13], J. Borrill[19,131], F. R. Bouchet[85,129], F. Boulanger[84], M. Bucher[1], R. Burenin[130,113], C. Burigana[70,47,72], R. C. Butler[70], E. Calabrese[135], J.-F. Cardoso[104,1,85], P. Carvalho[88,98], B. Casaponsa[92], G. Castex[1], A. Catalano[105,101], A. Challinor[88,98,17], A. Chamballu[103,21,84], R.-R. Chary[81], H. C. Chiang[39,10], J. Chluba[34,98], G. Chon[111], P. R. Christensen[117,53], S. Church[133], M. Clemens[67], D. L. Clements[80], S. Colombi[85,140], L. P. L. Colombo[33,95], C. Combet[105], B. Comis[105], D. Contreras[32], F. Couchot[100], A. Coulais[101], B. P. Crill[95,16], M. Cruz[27], A. Curto[92,9,98], F. Cuttaia[70], L. Danese[123], R. D. Davies[96], R. J. Davis[96], P. de Bernardis[48], A. de Rosa[70], G. de Zotti[67,123], J. Delabrouille[1], J.-M. Delouis[85,140], F.-X. Désert[77], E. Di Valentino[85,129], C. Dickinson[96], J. M. Diego[92], K. Dolag[145,110], H. Dole[84,83], S. Donzelli[71], O. Doré[95,16], M. Douspis[84], A. Ducout[85,80], J. Dunkley[135], X. Dupac[57], G. Efstathiou[98,88], P. R. M. Eisenhardt[95], F. Elsner[35,85,140], T. A. Enßlin[110], H. K. Eriksen[89], E. Falgarone[101], Y. Fantaye[52,5], M. Farhang[13,122], S. Feeney[80], J. Fergusson[17], R. Fernandez-Cobos[92], F. Feroz[9], F. Finelli[70,72], E. Florido[146], O. Forni[143,14], M. Frailis[69], A. A. Fraisse[39], C. Franceschet[49], E. Franceschi[70], A. Frejsel[117], A. Frolov[128], S. Galeotta[69], S. Galli[97], K. Ganga[1], C. Gauthier[1,109], R. T. Génova-Santos[91,25], M. Gerbino[138,119,48], T. Ghosh[84], M. Giard[143,14], Y. Giraud-Héraud[1], E. Giusarma[48], E. Gjerløw[89], J. González-Nuevo[26,92], K. M. Górski[95,150], K. J. B. Grainge[9,98], S. Gratton[98,88], A. Gregorio[50,69,76], A. Gruppuso[70,72], J. E. Gudmundsson[138,119,39], J. Hamann[139,136], W. Handley[98,9], F. K. Hansen[89], D. Hanson[112,95,13], D. L. Harrison[88,98], A. Heavens[80], G. Helou[16], S. Henrot-Versillé[100], C. Hernández-Monteagudo[18,110], D. Herranz[92], S. R. Hildebrandt[95,16], E. Hivon[85,140], M. Hobson[9], W. A. Holmes[95], A. Hornstrup[22], W. Hovest[110], Z. Huang[13], K. M. Huffenberger[37], G. Hurier[84], S. Ilić[143,14,8], A. H. Jaffe[80], T. R. Jaffe[143,14], T. Jin[9], W. C. Jones[39], M. Juvela[38], A. Karakci[1], E. Keihänen[38], R. Keskitalo[19], I. Khamitov[137,30], K. Kiiveri[38,64], J. Kim[110], T. S. Kisner[107], R. Kneissl[55,11], J. Knoche[110], L. Knox[42], N. Krachmalnicoff[49], M. Kunz[23,84,5], H. Kurki-Suonio[38,64], F. Lacasa[84,65], G. Lagache[7,84], A. Lähteenmäki[2,64], J.-M. Lamarre[101], M. Langer[84], A. Lasenby[9,98], M. Lattanzi[47,73], C. R. Lawrence[95,⋆], M. Le Jeune[1], J. P. Leahy[96], E. Lellouch[102], R. Leonardi[12], J. León-Tavares[90,59,3], J. Lesgourgues[86,139], F. Levrier[101], A. Lewis[36], M. Liguori[45,94], P. B. Lilje[89], M. Lilley[85,129], M. Linden-Vørnle[22], V. Lindholm[38,64], H. Liu[117,53], M. López-Caniego[57], P. M. Lubin[43], Y.-Z. Ma[96,125], J. F. Macías-Pérez[105], G. Maggio[69], D. Maino[49,71], D. S. Y. Mak[88,98], N. Mandolesi[70,47], A. Mangilli[84,100], A. Marchini[74], A. Marcos-Caballero[92], D. Marinucci[52], M. Maris[69], D. J. Marshall[103], P. G. Martin[13], M. Martinelli[148], E. Martínez-González[92], S. Masi[48], S. Matarrese[45,94,61], P. Mazzotta[51], J. D. McEwen[114], P. McGehee[81], S. Mei[60,142,16], P. R. Meinhold[43], A. Melchiorri[48,74], J.-B. Melin[21], L. Mendes[57], A. Mennella[49,71], M. Migliaccio[88,98], K. Mikkelsen[89], M. Millea[42], S. Mitra[79,95], M.-A. Miville-Deschênes[84,13], D. Molinari[47,70,73], A. Moneti[85], L. Montier[143,14], R. Moreno[102], G. Morgante[70], D. Mortlock[80], A. Moss[127], S. Mottet[85,129], M. Münchmeyer[85], D. Munshi[126], J. A. Murphy[115], A. Narimani[32], P. Naselsky[118,54], A. Nastasi[84], F. Nati[39], P. Natoli[47,6,73], M. Negrello[67], C. B. Netterfield[29], H. U. Nørgaard-Nielsen[22], F. Noviello[96], D. Novikov[108], I. Novikov[117,108], M. Olamaie[9], N. Oppermann[13], E. Orlando[149], C. A. Oxborrow[22], F. Paci[123], L. Pagano[48,74], F. Pajot[84], R. Paladini[81], S. Pandolfi[24], D. Paoletti[70,72], B. Partridge[63], F. Pasian[69], G. Patanchon[1], T. J. Pearson[16,81], M. Peel[96], H. V. Peiris[35], V.-M. Pelkonen[81], O. Perdereau[100], L. Perotto[105], Y. C. Perrott[9], F. Perrotta[123], V. Pettorino[62], F. Piacentini[48], M. Piat[1], E. Pierpaoli[33], D. Pietrobon[95], S. Plaszczynski[100], D. Pogosyan[40], E. Pointecouteau[143,14], G. Polenta[6,68], L. Popa[87], G. W. Pratt[103], G. Prézeau[16,95], S. Prunet[85,140], J.-L. Puget[84], J. P. Rachen[31,110], B. Racine[89], W. T. Reach[144], R. Rebolo[91,20,25], M. Reinecke[110], M. Remazeilles[96,84,1], C. Renault[105], A. Renzi[52,75], I. Ristorcelli[143,14], G. Rocha[95,16], M. Roman[1], E. Romelli[50,69], C. Rosset[1], M. Rossetti[49,71], A. Rotti[79], G. Roudier[1,101,95], B. Rouillé d'Orfeuil[100], M. Rowan-Robinson[80], J. A. Rubiño-Martín[91,25], B. Ruiz-Granados[146], C. Rumsey[9], B. Rusholme[81], N. Said[48], V. Salvatelli[48,8], L. Salvati[48], M. Sandri[70], H. S. Sanghera[88,98], D. Santos[105], R. D. E. Saunders[9], A. Sauvé[143,14], M. Savelainen[38,64], G. Savini[120], B. M. Schaefer[141], M. P. Schammel[9,93], D. Scott[32], M. D. Seiffert[95,16], P. Serra[84], E. P. S. Shellard[17], T. W. Shimwell[9,134], M. Shiraishi[45,94], K. Smith[121], T. Souradeep[79], L. D. Spencer[126], M. Spinelli[100], S. A. Stanford[42], D. Stern[95], V. Stolyarov[9,132,99], R. Stompor[1], A. W. Strong[111], R. Sudiwala[126], R. Sunyaev[110,130], P. Sutter[85], D. Sutton[88,98], A.-S. Suur-Uski[38,64], J.-F. Sygnet[85], J. A. Tauber[58], D. Tavagnacco[69,50], L. Terenzi[124,70], D. Texier[56], L. Toffolatti[26,92,70], M. Tomasi[49,71], M. Tornikoski[3], D. Tramonte[91,25], M. Tristram[100], A. Troja[49], T. Trombetti[70,47], M. Tucci[23], J. Tuovinen[15], M. Türler[78], G. Umana[66], L. Valenziano[70], J. Valiviita[38,64], F. Van Tent[106], T. Vassallo[69], L. Vibert[84], M. Vidal[96], M. Viel[69,76], P. Vielva[92], F. Villa[70], L. A. Wade[95], B. Walter[63], B. D. Wandelt[85,140,44], R. Watson[96], I. K. Wehus[95,89], N. Welikala[135], J. Weller[145], M. White[41], S. D. M. White[110], A. Wilkinson[96], D. Yvon[21], A. Zacchei[69], J. P. Zibin[32], and A. Zonca[43]

(Affiliations can be found after the references)

Received 1 August 2015 / Accepted 18 January 2016

ABSTRACT

The European Space Agency's *Planck* satellite, which is dedicated to studying the early Universe and its subsequent evolution, was launched on 14 May 2009. It scanned the microwave and submillimetre sky continuously between 12 August 2009 and 23 October 2013. In February 2015, ESA and the Planck Collaboration released the second set of cosmology products based on data from the entire *Planck* mission, including both temperature and polarization, along with a set of scientific and technical papers and a web-based explanatory supplement. This paper gives an overview of the main characteristics of the data and the data products in the release, as well as the associated cosmological and astrophysical science results and papers. The data products include maps of the cosmic microwave background (CMB), the thermal Sunyaev-Zeldovich effect, diffuse foregrounds in temperature and polarization, catalogues of compact Galactic and extragalactic sources (including separate catalogues of

⋆ Corresponding author: C. R. Lawrence, e-mail: charles.lawrence@jpl.nasa.gov

Sunyaev-Zeldovich clusters and Galactic cold clumps), and extensive simulations of signals and noise used in assessing uncertainties and the performance of the analysis methods. The likelihood code used to assess cosmological models against the *Planck* data is described, along with a CMB lensing likelihood. Scientific results include cosmological parameters derived from CMB power spectra, gravitational lensing, and cluster counts, as well as constraints on inflation, non-Gaussianity, primordial magnetic fields, dark energy, and modified gravity, and new results on low-frequency Galactic foregrounds.

Key words cosmology: observations – cosmic background radiation – surveys – space vehicles: instruments – instrumentation: detectors

1. Introduction

The *Planck* satellite[1] (Tauber et al. 2010; Planck Collaboration I 2011), launched on 14 May 2009, observed the sky continuously from 12 August 2009 to 23 October 2013. *Planck*'s scientific payload contained an array of 74 detectors in nine bands covering frequencies between 25 and 1000 GHz, which scanned the sky with angular resolution between 33′ and 5′. The detectors of the Low Frequency Instrument (LFI; Bersanelli et al. 2010; Mennella et al. 2011) were pseudo-correlation radiometers, covering bands centred at 30, 44, and 70 GHz. The detectors of the High Frequency Instrument (HFI; Lamarre et al. 2010; Planck HFI Core Team 2011) were bolometers, covering bands centred at 100, 143, 217, 353, 545, and 857 GHz. *Planck* imaged the whole sky twice in one year, with a combination of sensitivity, angular resolution, and frequency coverage never before achieved. *Planck*, its payload, and its performance as predicted at the time of launch are described in 13 papers included in a special issue of Astronomy & Astrophysics (Volume 520).

The main objective of *Planck*, defined in 1995, was to measure the spatial anisotropies in the temperature of the cosmic microwave background (CMB), with an accuracy set by fundamental astrophysical limits, thereby extracting essentially all the cosmological information embedded in the temperature anisotropies of the CMB. *Planck* was not initially designed to measure to high accuracy the CMB polarization anisotropies, which encode not only a wealth of cosmological information, but also provide a unique probe of the history of the Universe during the time when the first stars and galaxies formed. However, during *Planck*'s development it was significantly enhanced in this respect, and its polarization measurement capabilities have exceeded all original expectations. *Planck* was also designed to produce a wealth of information on the properties of extragalactic sources, including clusters of galaxies via the Sunyaev-Zeldovich (SZ) effect, and the dust and gas in the Milky Way. The scientific objectives of *Planck* were described in detail in Planck Collaboration (2005). With the results presented here and in a series of accompanying papers, *Planck* has already achieved all of its planned science goals.

An overview of the scientific operations of the *Planck* mission was given in Planck Collaboration I (2014). Further operational details extending to the end of the mission are presented in the 2015 Explanatory Supplement (Planck Collaboration 2015). The first set of scientific data, the Early Release Compact Source Catalogue (ERCSC; Planck Collaboration VII 2011), was released in January 2011. At the same time, a set of 26 papers related to astrophysical foregrounds were published in a special issue of Astronomy and Astrophysics (Vol. 536, 2011). Since then, 40 "Intermediate" (i.e., between the major data releases) papers have been submitted to A&A containing further astrophysical investigations by the Collaboration. The second set of scientific data (sometimes referred to as Planck Release 1 or "PR1", because it was the first release of cosmologically useful data) consisting mainly of temperature maps of the whole sky, was released in March of 2013. These data and associated scientific results are described in a set of 32 papers in another special issue of A&A (Vol. 571, 2014). This paper presents an overview of the third set of scientific data (and second set of cosmological data, hence "PR2") and scientific results to be released by *Planck*, based on the data acquired during the complete *Planck* mission from 12 August 2009 to 23 October 2013, and hereafter referred to as the "2015 products".

2. Data products in the 2015 release

The 2015 distribution of released products, freely accessible via the *Planck* Legacy Archive interface (PLA)[2], is based on all the data acquired by *Planck* during routine operations, starting on 12 August 2009 and ending on 23 October 2014. The distribution contains the following items.

- Cleaned and calibrated data timelines for each detector.
- Maps of the sky at nine frequencies (Sect. 7) in temperature, and at seven frequencies (30–353 GHz) in polarization. Additional products serve to quantify the characteristics of the maps to a level adequate for the science results being presented, such as noise maps, masks, and instrument characteristics.
- High-resolution maps of the CMB sky in temperature from four different component-separation approaches, and accompanying characterization products (Sect. 8.1).
- High-pass-filtered maps of the CMB sky in polarization from four different component-separation approaches, and accompanying characterization products (Sect. 8.1). The rationale for providing these maps is explained in Sect. 2.2.
- A low-resolution CMB temperature map (Sect. 8.1) used in the low-ℓ likelihood code, with an associated set of foreground temperature maps produced as part of the process of separating the low-resolution CMB from foregrounds, with accompanying characterization products.
- Maps of thermal dust and residual cosmic infrared background (CIB) fluctuations, as well as carbon monoxide (CO), synchrotron, free-free, and spinning dust temperature emission, plus maps of dust temperature and opacity (Sect. 9).
- Maps of synchrotron and dust polarized emission.
- A map of the estimated CMB lensing potential over 70% of the sky.
- A map of the SZ effect Compton parameter.
- Monte Carlo chains used in determining cosmological parameters from the *Planck* data.
- The Second Planck Catalogue of Compact Sources (PCCS2; Sect. 9.1), comprising lists of compact sources over the entire sky at the nine *Planck* frequencies. The PCCS2 includes polarization information, and supersedes the previous Early Release Compact Source Catalogue (Planck Collaboration XIV 2011) and the PCCS1 (Planck Collaboration XXVIII 2014).

[1] *Planck* (http://www.esa.int/Planck) is a project of the European Space Agency (ESA) with instruments provided by two scientific consortia funded by ESA member states and led by Principal Investigators from France and Italy, telescope reflectors provided through a collaboration between ESA and a scientific consortium led and funded by Denmark, and additional contributions from NASA (USA).

[2] http://pla.esac.esa.int

- The Second Planck Catalogue of Sunyaev-Zeldovich Sources (PSZ2; Sect. 9.2), comprising a list of sources detected by their SZ distortion of the CMB spectrum. The PSZ2 supersedes the previous Early Sunyaev-Zeldovich Catalogue (Planck Collaboration XXIX 2014) and the PSZ1 (Planck Collaboration XXIX 2014).
- The Planck Catalogue of Galactic Cold Clumps (PGCC; Planck Collaboration XXVIII 2016), providing a list of Galactic cold sources over the whole sky (see Sect. 9.3). The PGCC supersedes the previous Early Cold Core Catalogue (ECC), part of the Early Release Compact Source Catalogue (ERCSC; Planck Collaboration VII 2011).
- A full set of simulations, including Monte Carlo realizations.
- A likelihood code and data package used for testing cosmological models against the *Planck* data, including both the CMB (Sect. 8.4.1) and CMB lensing (Sect. 8.4.2).

The first 2015 products were released in February 2015, polarized maps and time-ordered data were released in July 2015, and simulations were released in September 2015 (see Sect. 4). In parallel, the Planck Collaboration is developing the next generation of data products, which will be delivered in 2016.

2.1. Polarization convention

The *Planck* Stokes parameter maps and data follow the "COSMO" [3] convention for polarization angles, rather than the "IAU" (Heeschen & Howard 1974; Hamaker & Bregman 1996) convention. The net effect of using the COSMO convention is a sign inversion on Stokes U with respect to the IAU convention (position angle increases clockwise in the IAU convention, anticlockwise in the IAU convention). On the other hand, when polarization angles are discussed in Planck Collaboration papers, they are given in the IAU convention (e.g., in the Planck Catalogue of Compact Sources, Planck Collaboration XXVIII 2014; the Second Planck Catalogue of Compact Sources, Planck Collaboration XXVI 2016; and papers on foregrounds), with position angle zero being the direction of the north Galactic pole. All *Planck* FITS files containing polarization data include a keyword (POLCCONV) that specifies the convention used, and the text and figures of papers also specify the convention. Users should be aware, however, of this potential source of confusion.

2.2. The state of polarization in the Planck 2015 data

LFI – The 2015 *Planck* release includes polarization data at 30, 44, and 70 GHz. The 70 GHz polarization data are used for the 2015 *Planck* likelihood at $\ell < 30$. The 70 GHz map is cleaned with the 30 and 353 GHz channels for synchrotron and dust emission, respectively (Planck Collaboration XIII 2016).

Control of systematic effects in polarization is a challenging task, especially at large angular scales. We analyse systematic effects in the 2015 LFI polarization data (Planck Collaboration III 2016) following two complementary paths. First, we use the redundancy in the *Planck* scanning strategy to produce difference maps that, in principle, contain the same sky signal ("null tests"). Any residuals in these maps blindly probe all non-common-mode systematics present in the data. Second, we use our knowledge of the instrument to build physical models of all relevant systematic effects. We then simulate timelines and project them into sky maps following the LFI map-making process. We quantify the results in terms of power spectra, and compare them to the FFP8 LFI noise model.

[3] See http://healpix.sourceforge.net/html/intronode6.htm.

Our analysis shows no evidence of systematic errors significantly affecting the 2015 LFI polarization results. On the other hand, our model indicates that at low multipoles the dominant LFI systematics (gain errors and ADC nonlinearity) are only marginally dominated by noise and the expected signal. Therefore, further independent tests are being carried out and will be discussed in a forthcoming paper, as well as in the final 2016 *Planck* release. These include polarization cross-spectra between the LFI 70 GHz and the HFI 100 and 143 GHz maps (that are not part of this 2015 release; see below). Because systematic effects between the two *Planck* instruments are expected to be largely uncorrelated, such a cross-instrument approach may prove particularly effective.

HFI – The February 2015 data release included polarization data at 30, 44, 70, and 353 GHz. The release of the remaining three polarized HFI channels – 100, 143, and 217 GHz – was delayed because of residual systematic errors in the polarization data, particularly but not exclusively at $\ell < 10$. The sources of these systematic errors were identified, but insufficiently characterized to support reliable scientific analyses of, for example, the optical depth to ionization τ and the isotropy and statistics of the polarization fluctuations. Due to an internal mixup, however, the unfiltered polarized sky maps ended up in the PLA instead of the high-pass-filtered ones. This was discovered in July 2015, and the high-pass-filtered maps at 100, 143, and 217 GHz were added to the PLA. The unfiltered maps have been left in place to avoid confusion, but warnings about their unsuitability for science have been added. Since February our knowledge of the causes of residual systematic errors and our characterization of the polarization maps have improved. Problems that users might encounter in the released 100–353 GHz maps include the following:

- Null tests on data splits indicate inconsistency of polarization measurements on large angular scales at a level much larger than our instrument noise model (see Fig. 10 of Planck Collaboration VIII 2016). The reasons for this are numerous and will be described in detail in a future paper.
- While analogue-to-digital converter (ADC) nonlinearity is corrected much better than in previous releases, some residual effects remain, particularly in the distortion of the dipole that leaks dipole power to higher spatial frequencies.
- Mismatches in bandpasses result in leakage of dust temperature to polarization, particularly on large angular scales.
- While the measured beam models are improved, main beam mismatches cause temperature-to-polarization leakage in the maps (see Fig. 17 of Planck Collaboration VII 2016). In producing the results given in the *Planck* 2015 release, we correct for this at the spectrum level (Planck Collaboration XI 2016), but the maps themselves contain this effect.

The component-separation work described in Sect. 9, Planck Collaboration IX (2016), and Planck Collaboration X (2016) was performed on all available data, and produced unprecedented full-sky polarization maps of foreground emission (Figs. 22 and 24), as well as maps of polarized CMB emission. The polarized CMB maps, derived using four independent component-separation methods, were the basis for quantitative statements about the level of residual polarization systematics and the conclusion that reliable science results could not be obtained from them on the largest angular scales.

Recent improvements in mapmaking methodology that reduce the level of residual systematic errors in the maps, especially at low multipoles, will be described in a future paper. A

more fundamental ongoing effort aimed at correcting systematic polarization effects in the time-ordered data will produce the final legacy *Planck* data, to be released in 2016.

3. Papers accompanying the 2015 release

The characteristics, processing, and analysis of the *Planck* data, as well as a number of scientific results, are described in a series of papers released with the data. The titles of the papers begin with "*Planck* 2015 results", followed by the specific titles below.

I. Overview of products and scientific results (*this paper*)

II. Low Frequency Instrument data processing

III. LFI systematic uncertainties

IV. LFI beams and window functions

V. LFI calibration

VI. LFI mapmaking

VII. High Frequency Instrument data processing: Time-ordered information and beam processing

VIII. High Frequency Instrument data processing: Calibration and maps

IX. Diffuse component separation: CMB maps

X. Diffuse component separation: Foreground maps

XI. CMB power spectra, likelihoods, and robustness of parameters

XII. Simulations

XIII. Cosmological parameters

XIV. Dark energy and modified gravity

XV. Gravitational lensing

XVI. Isotropy and statistics of the CMB

XVII. Constraints on primordial non-Gaussianity

XVIII. Background geometry and topology of the Universe

XIX. Constraints on primordial magnetic fields

XX. Constraints on inflation

XXI. The integrated Sachs-Wolfe effect

XXII. A map of the thermal Sunyaev-Zeldovich effect

XXIII. The thermal Sunyaev-Zeldovich effect–cosmic infrared background correlation

XXIV. Cosmology from Sunyaev-Zeldovich cluster counts

XXV. Diffuse low-frequency Galactic foregrounds

XXVI. The Second Planck Catalogue of Compact Sources

XXVII. The Second Planck Catalogue of Sunyaev-Zeldovich Sources

XXVIII. The Planck Catalogue of Galactic Cold Clumps

This paper contains an overview of the main aspects of the *Planck* project that have contributed to the 2015 release, and points to the papers that contain full descriptions. It proceeds as follows. Section 4 describes the simulations that have been generated to support the analysis of *Planck* data. Section 5 describes the basic processing steps leading to the generation of the *Planck* timelines. Section 6 describes the timelines themselves. Section 7 describes the generation of the nine *Planck* frequency maps and their characteristics. Section 8 describes the *Planck* 2015 products related to the cosmic microwave background, namely the CMB maps, the lensing products, and the likelihood code. Section 9 describes the *Planck* 2015 astrophysical products, including catalogues of compact sources and maps of diffuse foreground emission. Section 10 describes the main cosmological science results based on the 2015 CMB products. Section 11 describes some of the astrophysical results based on the 2015 data. Section 12 concludes with a summary and a look towards future *Planck* products.

4. Simulations

We simulated time-ordered information (TOI) for the full focal plane (FFP) for the nominal mission. The first five FFP realizations were less comprehensive and were primarily used for validation and verification of the *Planck* analysis codes and for cross-validation of the data processing centre (DPC) and FFP simulation pipelines. The first *Planck* cosmology results (Planck Collaboration I 2014) were supported primarily by the sixth FFP simulation set, FFP6. The current results were supported by the eighth FFP simulation set, FFP8, which is described in detail in Planck Collaboration XII (2016).

Each FFP simulation comprises a single "fiducial" realization (CMB, astrophysical foregrounds, and noise), together with separate Monte Carlo (MC) realizations of the CMB and noise. The CMB component contains the effect of our motion with respect to the CMB rest frame. This induces an additive dipolar aberration, a frequency-dependent dipole modulation, and a frequency-dependent quadrupole in the CMB data. Of these effects, the additive dipole and frequency-independent component of the quadrupole are removed (see Planck Collaboration XII 2016 for details), while the residual quadrupole and modulation effects are left in the simulations and are also left in the LFI and HFI data. The residual aberration contribution to the Doppler boosting was planned to be left in the simulations; however, due to a bug in the code generating the CMB realizations, it was inadvertently omitted. New, corrected, realizations are being generated, and will be added to the public data release when they become available. This effect remains in the LFI and HFI data.

To mimic the *Planck* data as closely as possible, the simulations use the actual pointing, data flags, detector bandpasses, beams, and noise properties of the nominal mission. For the fiducial realization, maps were made of the total observation (CMB, foregrounds, and noise) at each frequency for the nominal mission period, using the *Planck* Sky Model (Delabrouille et al. 2013). In addition, maps were made of each component separately, of subsets of detectors at each frequency, and of half-ring and single Survey subsets of the data. The noise and CMB Monte Carlo realization-sets also included both all and subsets of detectors (so-called "DetSets") at each frequency, and full and half-ring data sets for each detector combination.

To check that the 2015 results are not sensitive to the exact cosmological parameters used in FFP8, we subsequently generated FFP8.1, exactly matching the PR2 (2015) cosmology.

All of the FFP8 and FFP8.1 simulations are available to be used at NERSC[4]; in addition, a limited subset of the simulations is available for download from the PLA.

5. Data processing

5.1. Timeline processing

5.1.1. LFI

The main changes in LFI data processing compared to the earlier release (Planck Collaboration II 2014) are in how we account for beam information in the pipeline, and in calibration. Processing starts at Level 1, which retrieves necessary information from data packets and auxiliary data received from the Mission Operation

[4] http://crd.lbl.gov/cmb-data

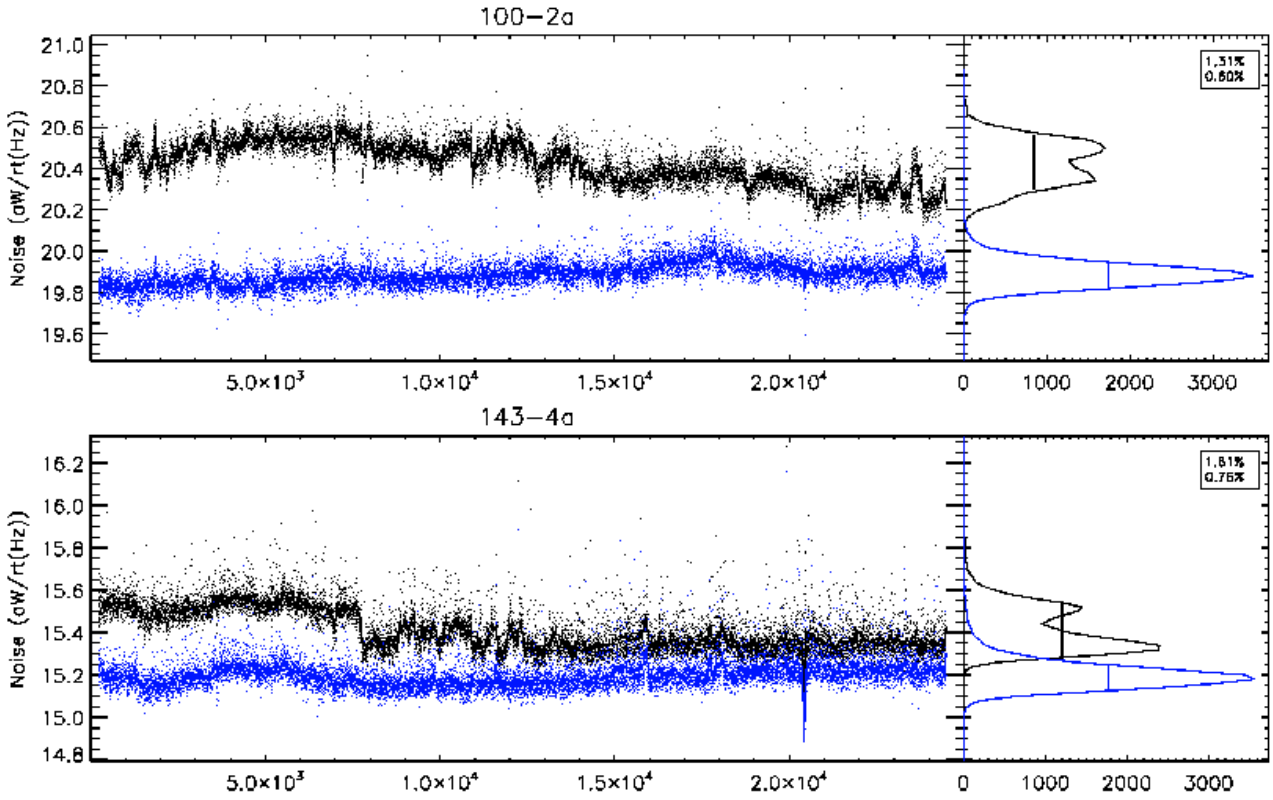

Fig. 1. *Left panels*: noise for two bolometers as a function of ring number. Black dots are from the 2013 data release; blue dots are from the 2015 release. The change in the absolute noise level is due to a change in the time-response deconvolution between the two data releases. *Right panels*: histograms of the noise. The numbers in the boxes give the width of the histogram at half maximum as a percentage of the mean noise level. For most bolometers, the FWHM in the 2015 release is less than 1% (Planck Collaboration VIII 2016).

Centre, and transforms the scientific packets and housekeeping data into a form manageable by Level 2. Level 2 uses scientific and housekeeping information to:

- build the LFI reduced instrument model (RIMO), which contains the main characteristics of the instrument;
- remove ADC nonlinearities and 1 Hz spikes diode by diode;
- compute and apply the gain modulation factor to minimize $1/f$ noise;
- combine signals from the diodes with associated weights;
- compute the appropriate detector pointing for each sample, based on auxiliary data and beam information, corrected by a model (PTCOR) built using Solar distance and radiometer electronics box assembly (REBA) temperature information;
- calibrate the scientific timelines in physical units (K_{CMB}), fitting the total CMB dipole convolved with the 4π beam representation, without taking into account the signature due to Galactic stray light;
- remove the Solar and orbital dipoles (convolved with the 4π beam) and the Galactic emission (convolved with the beam sidelobes) from the scientific calibrated timeline; and
- combine the calibrated time-ordered information (TOI) into aggregate products, such as maps at each frequency.

Level 3 collects Level 2 outputs from both LFI and HFI (Planck Collaboration VI 2016; Planck Collaboration VIII 2016) and derives various products, such as component-separated maps of astrophysical foregrounds, catalogues of different classes of source, and the likelihood of cosmological and astrophysical models given in the maps.

5.1.2. HFI

The most important change in HFI data processing compared to the 2013 release (Planck Collaboration VI 2014) is in the very first step of the pipeline, namely correction of nonlinearity in the 16-bit analogue-to-digital converters (ADCs) that are the last component in the bolometer readout electronics (Planck Collaboration 2015). The subtle effects of the ADC nonlinearities that mimic gain variations were neither detected in ground tests nor anticipated before flight, but proved to be the source of the most difficult systematic errors to deal with in the flight data. A method that reduces the effects of ADC nonlinearity by more than an order of magnitude for most channels has been implemented. Improvements can be assessed by comparing the noise stationarity in the 2013 and the 2015 data (Fig. 1). There is a significant decrease in the width of the noise distributions when the ADC correction is included.

Several other changes were also made in processing for the 2015 release. For strong signals, the threshold for cosmic ray removal ("deglitching") is auto-adjusted to cope with signal variations near bright sources caused by small pointing drifts during a ring. Thus, more glitches are left in the data in the vicinity of bright sources such as the Galactic centre than are left elsewhere. To mitigate this effect, the TOI at the planet locations are flagged and interpolated prior to further processing. For the 2015 release, this is done for Jupiter at all HFI frequency bands, for Saturn at $\nu \geq 217$ GHz, and for Mars at $\nu \geq 353$ GHz. For beam determination and calibration (see Sect. 5.2.2 of Planck Collaboration VII 2016 and Planck Collaboration VIII 2016), however, the full TOI at all planet crossings are needed at all frequencies. To recover these

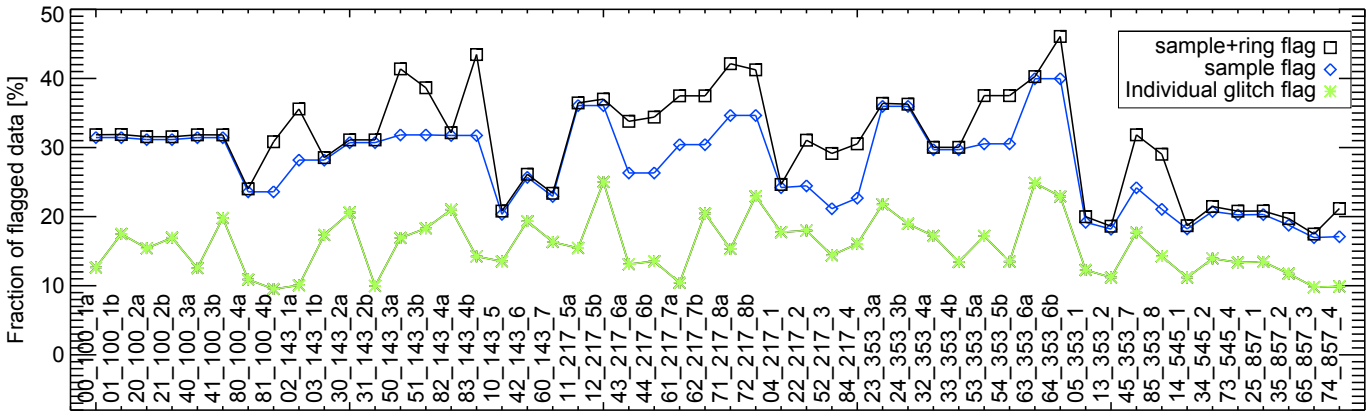

Fig. 2. Fraction of discarded data per bolometer due to all causes (black squares), sample flagging alone (blue diamonds) and glitches alone (green diamonds). Bolometers (143_8 and 545_3) are not shown, since they are not used in the data processing (see Planck Collaboration VI 2014).

data in 2015, a specialized, iterative, 3-level deglitcher is run in parallel on TOI in the vicinity of strong sources.

As noted in Planck Collaboration I (2014), *Planck* scans a given ring on the sky for between 39 and 65 min before moving on to the next ring. The data between these rings, taken while the spacecraft spin-axis is moving, are discarded as "unstable". The data taken during the intervening "stable" periods are subjected to a number of statistical tests to decide whether they should be flagged as usable or not (Planck Collaboration VI 2014). This procedure continues to be used for the present data release. An additional selection process has been introduced to mitigate the effect of interference from the 4-K cooler electronics on the data, especially the 30-Hz line signal that is correlated across bolometers. The 4-K line-removal procedure leaves correlated residuals in the 30-Hz line. The consequence of these correlations is that the angular cross-power spectra between different detectors can show excess power at multipoles around $\ell \approx 1800$ (see Sect. 10.1). To mitigate this effect, we discard all 30-Hz resonant rings for the 16 bolometers between 100 and 353 GHz for which the median average of the 30-Hz line amplitude is above 10 aW. As a result, the $\ell \approx 1800$ feature is greatly suppressed.

No other changes were made in the TOI processing software, apart from fine-tuning of several input parameters for better control of residual systematic errors noticed in the 2013 data.

Figure 2 shows the fraction of data discarded per bolometer over the full mission. Black squares show the fraction discarded due to all causes, including glitches, spin-axis repointings (8%), station-keeping manoeuvres, 4-K cooler lines, Solar flares, and end-of-life calibration sequences. Green stars show the fraction discarded due to glitches alone. Blue diamonds show the fraction discarded in rings that have some valid data, i.e., rings not flagged as entirely bad with the "ring flag". (Note that spin-axis repointing and station-keeping manoeuvres are not part of rings, and therefore never flagged as rings.) Green stars show the fraction discarded due to glitches alone. Compared to flagging in the nominal mission, presented in the 2013 papers, the main differences appear in Survey 5, which is affected by Solar flares arising from increased Solar activity, and to special calibration sequences. The full cold *Planck* HFI mission lasted 885 days, excluding the calibration and performance verification (CPV) period of 1.5 months. Globally, for this duration, the total amount of HFI data discarded amounted to 31%, about half of which came from glitch flagging.

5.2. Beams

5.2.1. LFI beams

As described in Planck Collaboration IV (2016), the in-flight assessment of the LFI main beams relied on measurements of seven Jupiter crossings: the first four occurred in nominal scan mode (spin shift 2′, 1° day^{-1}); and the last three scans in "deep" mode (spin shift 0.′5, 15′ day^{-1}). By stacking data from the seven scans, the main beam profiles are measured down to −25 dB at 30 and 44 GHz, and down to −30 dB at 70 GHz. Fitting the main beam shapes with an elliptical Gaussian profile, we have expressed the uncertainties of the measured scanning beams in terms of statistical errors for the Gaussian parameters: ellipticity; orientation; and FWHM. In this release, the error on the reconstructed beam parameters is lower than that in the 2013 release. Consequently, the error envelope on the window functions is lower as well. For example, the beam FWHM is determined with a typical uncertainty of 0.2% at 30 and 44 GHz, and 0.1% at 70 GHz, i.e., a factor of two better than the value achieved in 2013.

The scanning beams[5] used in the LFI pipeline (affecting calibration, effective beams, and beam window functions) are based on GRASP simulations, properly smeared to take into account the satellite motion, and are similar to those presented in Planck Collaboration IV (2014). They come from a tuned optical model, and represent a realistic fit to the available measurements of the LFI main beams. In Planck Collaboration IV (2014), calibration was performed assuming a pencil beam, the main beams were full-power main beams, and the resulting beam window functions were normalized to unity. For the 2015 release, a different beam normalization has been used to properly take into account the fact that not all power enters through the main beam (typically about 99% of the total power is in the main beam). As described in Planck Collaboration V (2016), the current LFI calibration takes into account the full 4π beam (i.e., the main beam, as well as near and far sidelobes). Consequently, in the

[5] The term "scanning beam" refers to the angular response of a single detector to a compact source, including the optical beam, the smearing effect of scanning plus sampling, and (for HFI) residuals of the complicated time response of the detectors and electronics. In the case of HFI, a Fourier filter deconvolves the bolometer/electronics time response and lowpass-filters the data. The term "effective beam" refers to a beam defined in the map domain, obtained by averaging the scanning beams pointing at a given pixel of the sky map, taking into account the scanning strategy and the orientation of the beams themselves when they point along the direction to that pixel (Planck Collaboration IV 2014).

calculation of the window function, the beams are not normalized to unity; instead, their normalization uses the value of the efficiency calculated taking into account the variation across the band of the optical response (coupling between feedhorn pattern and telescope) and the radiometric response (band shape).

Although the GRASP beams are computed as the far-field angular transmission function of a linearly polarized radiating element in the focal plane, the far-field pattern is in general not perfectly linearly polarized, because there is a spurious component induced by the optical system, called "beam cross-polarization". The Jupiter scans allowed us to measure only the total field, that is, the co- and cross-polar components combined in quadrature. The adopted beam model has the added value of defining the co- and cross-polar pattern separately, and it permits us to properly consider the beam cross-polarization in every step of the LFI pipeline. The GRASP model, together with the pointing information derived from the reconstruction of the focal plane geometry, gives the most advanced and precise noise-free representation of the LFI beams.

The polarized main beam models were used to calculate the effective beams, which take into account the specific scanning strategy and include any smearing and orientation effects on the beams themselves. Moreover, the sidelobes were used in the calibration pipeline to correctly evaluate the gains and to subtract Galactic stray light from the calibrated timelines (Planck Collaboration II 2016).

To evaluate the beam window functions, we adopted two independent approaches, both based on Monte Carlo simulations. In one case, we convolved a fiducial CMB signal with realistic scanning beams in harmonic space to generate the corresponding timelines and maps. In the other case, we convolved the fiducial CMB map with effective beams in pixel space using the FEBeCoP (Mitra et al. 2011) method. Using the first approach, we have also evaluated the contribution of the near and far sidelobes on the window functions. The impact of sidelobes on low multipoles is about 0.1% (for details see Planck Collaboration IV 2016).

The error budget was evaluated as in the 2013 release, and comes from two contributions: the propagation of the main beam uncertainties throughout the analysis; and the contribution of near and far sidelobes in the Monte Carlo simulation chain. Which of the two sources of error dominates depends on the angular scale. Ignoring the near and far sidelobes is the dominant error at low multipoles, while the main beam uncertainties dominate the total error budget at $\ell \geq 600$. The total uncertainties in the effective beam window functions are 0.4% at 30 GHz, 1% at 44 GHz (both at $\ell \approx 600$), and 0.3% at 70 GHz (at $\ell \approx 1000$).

5.2.2. HFI beams

Measurement of the HFI main beams is described in detail in Planck Collaboration VII (2016), and is similar to that of Planck Collaboration VII (2014) but with several important changes. The HFI scanning beam model is a "Bspline" decomposition of the time-ordered data from planetary observations. The domain of reconstruction of the main beam in 2015 is enlarged from a 40′ square to a 100′ square, and is no longer apodized, in order to preserve near sidelobe structure Planck Collaboration XXXI (2014) and to incorporate residual time-response effects into the beam model. A combination of Saturn and Jupiter data is used instead of Mars data for improved signal-to-noise ratio, and a simple model of diffraction consistent with physical optics predictions is used to extend the beam model below the noise floor of the planetary data. Additionally, a second stage of cosmic ray glitch removal is added to reduce bias from unflagged cosmic ray hits.

The effective beams and effective beam window functions are computed using the FEBeCoP and Quickbeam codes, as in Planck Collaboration VII (2014). While the scanning beam measurement produces a total intensity map only, effective beam window functions appropriate for both temperature and polarized angular power spectra are produced by averaging the individual detector window functions, weighted by temperature and polarization sensitivity. Temperature-to-polarization leakage due to main beam mismatch is subdominant to noise in the polarization measurement, and is corrected as an additional nuisance parameter in the likelihood.

Uncertainties in the beam measurements are derived from an ensemble of 100 Monte Carlo simulations of planet observations, which include random realizations of detector noise, cosmic ray hits, and pointing uncertainties propagated through the same pipeline as the data. The errors are expressed in multipole space as a set of error eigenmodes, which capture the correlation structure of the errors. Additional checks are performed to validate the error model, such as splitting up the planet data to construct Year 1 and Year 2 beams and comparison with Mars-based beams. With improved control of systematics and higher signal-to-noise ratio, the uncertainties in the HFI beam window functions have decreased by more than a factor of 10 relative to the 2013 release.

Several differences between the beams in 2013 and 2015 may be highlighted.

- *Finer polar grid.* Instead of the Cartesian grid 40′ on each side used previously, the beam maps were produced on both a Cartesian grid of 200′ on each side and 2″ resolution, and a polar grid with a radius of 100′ and a resolution of 2″ in radius and 30′ in azimuth. The latter grid has the advantage of not requiring any extra interpolation to compute the beam spherical harmonic coefficients $b_{\ell m}$ required by quickbeam, and therefore improves the accuracy of the resulting $B(\ell)$.
- *Scanning beam elongation.* To account for the elongation of the scanning beam induced by the residuals of the time-response deconvolution, quickbeam uses the $b_{\ell m}$ over the range $-6 \leq m \leq 6$. We checked that the missing terms account for less than 10^{-4} of the effective $B^2(\ell)$ at $\ell = 2000$. Moreover, comparisons with the effective $B(\ell)$ obtained by FEBeCoP show very good agreement.
- *Finite size of Saturn.* Even though its rings seem invisible at *Planck* frequencies, Saturn has an angular size that must be accounted for in the beam window function. The planet was assumed to be a top-hat disc of radius 9.″5 at all HFI frequencies, whose window function is well approximated by that of a 2D Gaussian profile of FWHM 11.″185. The effective $B(\ell)$s were therefore divided by that window function.
- *Cut sky and pixel shape variability.* The effective beam window functions do not include the (nominal) pixel window function, which must be accounted for separately in the analysis of *Planck* maps. However, the shapes and individual window functions of the HEALPix (Górski et al. 2005) pixels have large-scale variations around their nominal values across the sky. These variations affect the effective beam window functions applicable to *Planck* maps, in which the Galactic plane has been masked more or less conservatively, and are included in the effective $B(\ell)$s that are provided.
- *Polarization and detector weights.* Each 143, 217, and 353 GHz frequency map is a combination of measurements

by polarization-sensitive and polarization-insensitive detectors, each having a different optical response. As a consequence, at each of these frequencies, the Q and U maps will have a different beam window function than the I map. When cross-correlating the 143 and 217 GHz maps, for example, the TT, EE, TE, and ET spectra will each have a different beam window function.

- *Polarization and beam mismatch.* Since polarization measurements are differential by nature, any mismatch in the effective beams of the detectors involved will couple with temperature anisotropies to create spurious polarization signals (e.g., Hu et al. 2003; Leahy et al. 2010). In the likelihood pipeline (Planck Collaboration XI 2016), this additive leakage is modelled as a polynomial whose parameters are fitted to the power spectra.
- *Beam error model.* The improved S/N compared to 2013 leads to smaller uncertainties. At $\ell = 1000$ the uncertainties on B_ℓ^2 are 2.2×10^{-4}, 0.84×10^{-4}, and 0.81×10^{-4} for 100, 143, and 217 GHz, respectively. At $\ell = 2000$, they are 11×10^{-4}, 1.9×10^{-4}, and 1.3×10^{-4}.

A reduced instrument model (RIMO) containing the effective $B(\ell)$ for temperature and polarization detector assemblies is provided in the PLA for both auto- and cross-spectra. The RIMO also contains the beam error eigenmodes and their covariance matrices.

5.3. Focal plane geometry and pointing

The focal plane geometry of LFI was determined independently for each Jupiter crossing (Planck Collaboration IV 2016), using the same procedure adopted in the 2013 release. The solutions for the seven crossings agree within 4′ at 70 GHz (and 7′ at 30 and 44 GHz). The uncertainty in the determination of the main beam pointing directions evaluated from the single scans is about 4′ for the nominal scans, and 2.′5 for the deep scans at 70 GHz (27′ for the nominal scan and 19′ for the deep scan, at 30 and 44 GHz). Stacking the seven Jupiter transits, the uncertainty in the reconstructed main beam pointing directions becomes 0.′6 at 70 GHz, and 2′ at 30 and 44 GHz. With respect to the 2013 release, we have found a difference in the main beam pointing directions of about 5′ in the cross-scan direction and 0.′6 in the in-scan direction.

Throughout the extended mission, *Planck* continued to operate star camera STR1, with the redundant unit, STR2, used only briefly for testing. No changes were made to the basic attitude reconstruction. We explored the possibility of updating the satellite dynamical model and using the fibre-optic gyro for additional high frequency attitude information. Neither provided significant improvements to the pointing and were actually detrimental to overall pointing performance; however, they may become useful in future attempts to recover accurate pointing during the "unstable" periods.

Attitude reconstruction delivers two quantities, the satellite body reference system attitude, and the angles between it and the principal axis reference system (so-called "tilt" or "wobble" angles). The tilt angles are needed to reconstruct the focal plane line-of-sight from the raw body reference frame attitude. At the start of the LFI-only extension about 1000 days after launch, for unknown reasons the reconstructed tilt angles (cf. Fig. 3) began a drift that covered 1.′5 over about a month of operations. The drift was not seen in observed planet positions, and we were therefore forced to abandon the reconstructed tilt angles and include the tilt correction into our ad hoc pointing correction, PTCOR.

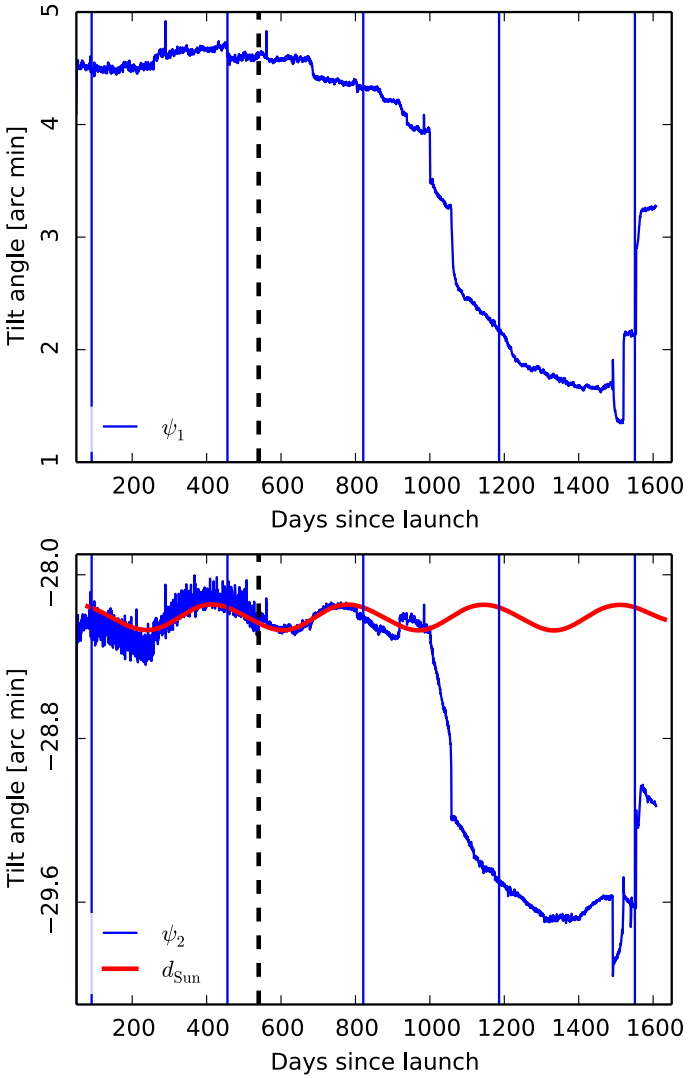

Fig. 3. Reconstructed tilt (wobble) angles between the satellite body frame and the principal axis frame. Vertical blue lines mark the boundaries of operational years, and the dashed black line indicates day 540 after launch, when the thermal control on the LFI radiometer electronics box assembly (REBA) was adjusted. *Top*: first tilt angle, ψ_1, which corresponds to a rotation about the satellite axis just 5° off the focal plane centre. Observed changes in ψ_1 have only a small effect on the focal plane line-of-sight. *Bottom*: second tilt angle, ψ_2, which is perpendicular to a plane defined by the nominal spin axis and the telescope line of sight. Rotation in ψ_2 immediately impacts the opening angle and thus the cross-scan position of the focal plane. We also plot a scaled and translated version of the Solar distance that correlates well with ψ_2 until the reconstructed angles became compromised about 1000 days after launch.

We noticed that the most significant tilt angle corrections prior to the LFI extension tracked well the distance $d_{\rm Sun}$ between the Sun and *Planck* (see Fig. 3, bottom panel), so we decided to replace the spline fitting from 2013 with the use of the Solar distance as a fitting template. The fit was improved by adding a linear drift component and inserting breaks at events known to disturb the spacecraft thermal environment. In Fig. 4 we show the co- and cross-scan pointing corrections, and a selection of planet position offsets after the correction was applied. The template-based pointing correction differs only marginally from the 2013 PTCOR, but an update was certainly necessary to provide consistent, high-fidelity pointing for the entire *Planck* mission.

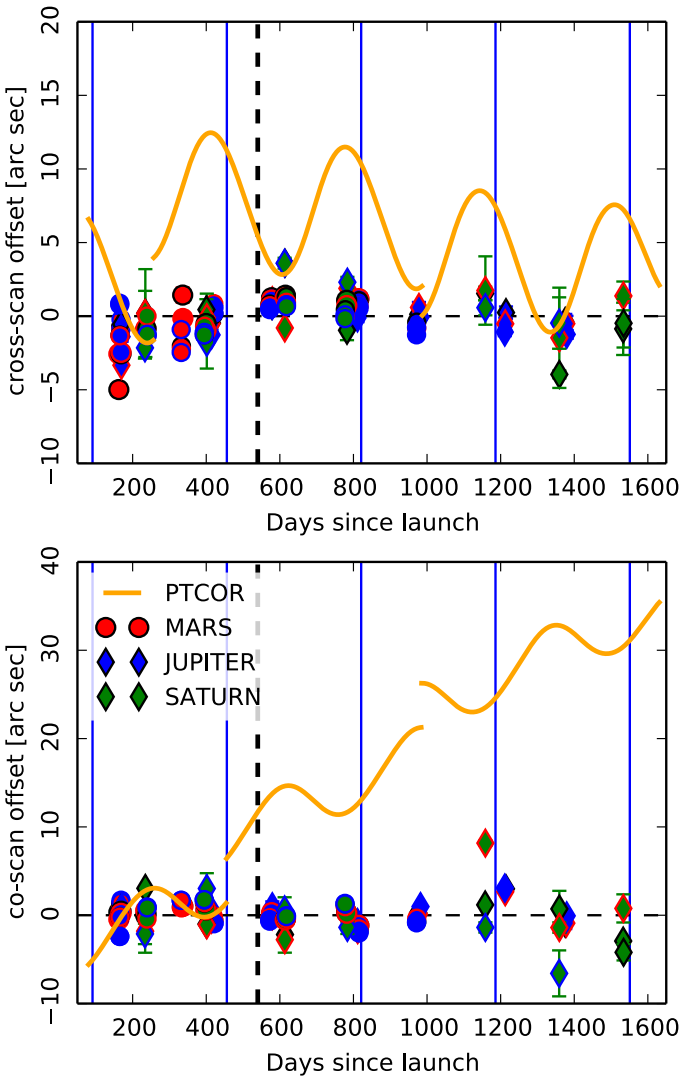

Fig. 4. PTCOR pointing correction, and a selection of observed planet position offsets after applying the correction. *Top*: cross-scan pointing offset. This angle is directly affected by the second tilt angle, ψ_2, discussed in Fig. 3. *Bottom*: in-scan pointing offset. This angle corresponds to the spin phase and matches the third satellite tilt angle, ψ_3. Since ψ_3 is poorly resolved by standard attitude reconstruction, the in-scan pointing was already driven by PTCOR in the 2013 release.

Finally, we addressed the LFI radiometer electronics box assembly (REBA) interference that was observed in the 2013 release, by constructing, fitting, and subtracting another template based on the REBA thermometry. This greatly reduced short-timescale pointing errors encountered prior to REBA thermal tuning on day 540. The REBA template-removal procedure reduced the pointing period timescale errors from 2.″7 to 0.″8 (in-scan) and 1.″9 (cross-scan).

5.4. Calibration

In this section we compare the relative photometric calibration of the all-sky CMB maps between LFI and HFI, as well as between *Planck* and WMAP. The two *Planck* instruments use different technologies and are subject to different foregrounds and systematic effects. The *Planck* and WMAP measurements overlap in frequency range, but have independent spacecraft, telescopes, and scanning strategies. Consistency tests between these three data sets are very demanding tests of the control of calibration, transfer functions, systematic effects, and foreground contamination.

5.4.1. The orbital dipole

In the 2013 data release, photometric calibration from 30 to 353 GHz was based on the "Solar dipole", that is, the dipole induced in the CMB by the motion of the Solar System barycentre with respect to the CMB. We used the value of the dipole measured by WMAP5 (Hinshaw et al. 2009; Jarosik et al. 2011).

In the 2015 data release, photometric calibration of both LFI and HFI is based on the "orbital dipole", i.e., the modulation of the Solar dipole induced by the orbital motion of the satellite around the Solar System barycentre. By using this primary calibrator, we can derive for each *Planck* detector (or combination of detectors) an independent measurement of the Solar dipole, which is then used in the *Planck* calibration pipeline. The orbital motion is known with exquisite accuracy, making the orbital dipole potentially the most accurate absolute calibration source in all of astrophysics, limited ultimately by the accuracy of the temperature of the CMB. The amplitude of this modulation, however, is only about 250 μK (varying with the details of the satellite motion), an order of magnitude smaller than the Solar dipole. Realizing its advantages as a fundamental calibration source requires low noise and good control of foregrounds, sidelobes, and large-angular-scale systematics. For the 2015 release, improvements in the control of systematic effects and foregrounds for both LFI and HFI, including the availability of 2.5 and 4 orbital cycles for HFI and LFI, respectively (compared to 1.25 cycles in the 2013 release), have allowed accurate calibration of both instruments on the orbital dipole, summarized in the following subsections and described in detail in Planck Collaboration II (2016) and Planck Collaboration VIII (2016). The dipole component of the CMB and the frequency-independent part of the quadrupole (induced by the Solar dipole) are removed from both the LFI and HFI data; however, higher-order effects of the Solar dipole (see Planck Collaboration XXVII 2014) are left in the data, as is also the case for the simulations described in Planck Collaboration XII (2016).

With the 2015 data calibrated on the orbital dipole, *Planck* has made independent measurements of the Solar dipole (Table 1), which can be compared to the WMAP5 measurement (Hinshaw et al. 2009). Amplitudes agree within 0.28%; directions agree to better than 2′. Although the difference in amplitude between the *Planck* and the WMAP5 measurements of the Solar dipole is small and within uncertainties, it had non-negligible consequences in 2013. WMAP was calibrated on the orbital dipole, so errors in its Solar dipole measurement did not contribute to its overall calibration errors. *Planck* in 2013, however, was calibrated on the WMAP5 Solar dipole, which is 0.28% lower than the orbital-dipole-calibrated 2015 *Planck* measurement. Calibrating LFI and HFI against WMAP5 in the 2013 results, therefore, resulted in 2013 gains that were 0.28% *too low* for both LFI and HFI. This factor is included in Tables 2 and 3.

5.4.2. Instrument level calibration

LFI – There were four significant changes related to LFI calibration between the 2013 and the 2015 results. First (as anticipated in the 2013 LFI calibration paper, Planck Collaboration V 2014), the convolution of the beam with the overall dipole (Solar

Table 1. LFI, HFI, and WMAP measurements of the Solar dipole.

Experiment	Amplitude [μK_{CMB}]	Galactic coordinates l [deg]	Galactic coordinates b [deg]
LFI[a]	3365.5 ± 3.0	264.01 ± 0.05	48.26 ± 0.02
HFI[a]	3364.29 ± 1.1	263.914 ± 0.013	48.265 ± 0.002
Planck 2015 nominal[a]	**3364.5 ± 2.0[b]**	**264.00 ± 0.03**	**48.24 ± 0.02**
WMAP[c]	3355[d] ± 8	263.99 ± 0.14	48.26 ± 0.03

Notes. [(a)] The "nominal" *Planck* dipole was chosen as a plausible combination of the LFI and HFI measurements early in the analysis, to carry out subtraction of the dipole from the frequency maps (see Sect. 5.4.3). The current best determination of the dipole comes from an average of 100 and 143 GHz results (Planck Collaboration VIII 2016). [(b)] Uncertainties include an estimate of systematic errors. [(c)] Hinshaw et al. (2009). [(d)] See Sect. 5.4.1 for the effect of this amplitude on *Planck* calibration in 2013.

Table 2. LFI calibration changes at map level, 2013 → 2015.

Frequency [GHz]	Beam solid angle [%]	Pipeline improvements[a] [%]	Orbital dipole[b] [%]	Total [%]
30	+0.32	−0.15	+0.28	+0.45
44	+0.03	+0.33	+0.28	+0.64
70	+0.30	+0.24	+0.28	+0.82

Notes. [(a)] This term includes the combined effect of the new destriping code, subtraction of Galactic contamination from timelines, and a new gain smoothing algorithm. It has been calculated under the simplifying assumption that it is fully independent of the beam convolution. [(b)] Change from not being dependent on the amplitude error of the WMAP9 Solar dipole (Sect. 5.4.1).

and orbital dipoles, including their induced frequency independent quadrupoles) is performed with the full 4π beam rather than a pencil beam. This dipole model is used to extract the gain calibration parameter. Because the details of the beam pattern are unique for each detector even within the same frequency channel, the reference signal used for the calibration is different for each of the 22 LFI radiometers. This change improves the results of null tests and the quality of the polarization maps. When taking into account the proper window functions (Planck Collaboration IV 2016), the new convolution scheme leads to shifts of +0.32, +0.03, and +0.30% in gain calibration at 30, 44, and 70 GHz, respectively (see Table 2). Second, a new destriping code, `Da Capo` (Planck Collaboration V 2016), is used; this supersedes the combination of a dipole-fitting routine and the `Mademoiselle` code used in the 2013 data release and offers improved handing of $1/f$ noise and residual Galactic signals. Third, Galactic contamination entering via sidelobes is subtracted from the timelines after calibration. Finally, a new smoothing algorithm is applied to the calibration parameters. It adapts the length of the smoothing window depending on a number of parameters, including the peak-to-peak amplitude of the dipole seen within each ring and sudden temperature changes in the instrument. These changes improve the results of null tests, and also lead to overall shifts in gain calibration a few tenths of a percent, depending on frequency channel. The values reported in the third column of Table 2 are approximate estimates from the combination of improved destriping, Galactic contamination removal, and smoothing. They are calculated under the simplifying assumption that these effects are completely independent of the beam convolution and can therefore be combined linearly with the latter (for more details see Planck Collaboration V 2016).

In total, these four improvements give an overall increase in gain calibration for LFI of +0.17, +0.36, and +0.54% at 30, 44, and 70 GHz, respectively. Adding the 0.28% error introduced by the WMAP Solar dipole in 2013 (discussed in Sect. 5.4.1), for the three LFI frequency channels we find overall shifts of about 0.5, 0.6 and 0.8% in gain calibration with respect to our LFI 2013 analysis (see Table 2).

As shown in Planck Collaboration V (2016), relative calibration between LFI radiometer pairs is consistent within their statistical uncertainties. At 70 GHz, using the deviations of the calibration of single channels, we estimate that the relative calibration error is about 0.1%.

HFI – There were three significant changes related to HFI calibration between the 2013 and the 2015 results: improved determination and handling of near and far sidelobes; improved ADC nonlinearity correction; and improved handling of very long time constants. The most significant changes arise from the introduction of near sidelobes of the main beam in the range of angles 0.°5 to 5°, and from the introduction of very long time constants. We consider these in turn.

Observations of Jupiter were not used in the 2013 results, because its signal is so strong that it saturates some stages of the readout electronics. The overall transfer function for each detector is corrected through the deconvolution of a time transfer function, leaving a compact effective beam that is used together with the maps in the science analysis. In the subsequent "consistency paper" (Planck Collaboration XXXI 2014), it was found that lower-noise hybrid beams built using observations of Mars, Saturn, and Jupiter reveal near sidelobes leading to significant corrections of 0.1 to 0.3%. Far sidelobes give a very small calibration correction that is almost constant for $\ell > 3$. The zodiacal contribution was removed in the timelines, since it does not project properly on the sky; it gives an even smaller and negligible correction except in the submillimetre channels at 545 and 857 GHz.

The most significant change results from the recognition of the existence of very long time constants (VLTC) and their inclusion in the analysis. VLTCs introduce a significant shift in the apparent position of the dominant anisotropy in the CMB, the Solar dipole, away from its true position. This in effect creates a leakage of the Solar dipole into the orbital dipole. This is the reason why calibration on the orbital dipole did not work as expected from simulations, and why calibration in 2013 was instead based on the WMAP5 Solar dipole. As discussed in

Table 3. HFI calibration changes at map level, 2013 → 2015.

	Sidelobes		Orbital dipole		
Frequency	Near	Far	Dipole[a]	VLTC	Total
[GHz]	[%]	[%]	[%]	[%]	[%]
100	0.2	0.087	0.28	0.49	1.06
143	0.2	0.046	0.28	0.47	1.00
217	0.2	0.043	0.28	0.66	1.17
353	0.275	0.006	0.28	1.5	2.06

Notes. [(a)] Change from not being dependent on the amplitude error of the WMAP9 Solar dipole (Sect. 5.4.1).

Sect. 5.4.1, the WMAP5 Solar dipole was underestimated by 0.28% when compared with the *Planck* best-measured amplitude, leading to an under-calibration of 0.28% in the *Planck* 2013 maps. With VLTCs included in the analysis, calibration on the orbital dipole worked as expected, and gave more accurate results, while at the same time eliminating the need to adopt the WMAP5 Solar dipole and removing the 0.28% error that it introduced in 2013.

These HFI calibration changes are summarized in Table 3. Together, they give an average shift of gain calibration of typically 1% (Planck Collaboration VIII 2016) for the three CMB channels, accounting for the previously unexplained difference in calibration on the first acoustic peak observed between HFI and WMAP.

The relative calibration between detectors operating at the same frequency is within 0.05% for 100 and 143 GHz, 0.1% at 217 GHz, and 0.4% at 353 GHz (Planck Collaboration VIII 2016). These levels for the CMB channels are within a factor of 3 of the accuracy floor set by noise in the low-ℓ polarization (Tristram et al. 2011).

The 545 and 857 GHz channels are calibrated separately using models of planetary atmospheric emission. As in 2013, we used both Neptune and Uranus. The main difference comes from better handling of the systematic errors affecting the planet flux density measurements. Analysis is now performed on the timelines, using aperture photometry, and taking into account the inhomogeneous spatial distribution of the samples. For the frequency maps, we estimate statistical errors on absolute calibration of 1.1% and 1.4% at 545 and 857 GHz, respectively, to which we add the 5% systematic uncertainty arising from the planet models. Errors on absolute calibration are therefore 6.1 and 6.4% at 545 and 857 GHz, respectively. Since the reported relative uncertainty of the models is of the order of 2%, we find the relative calibration between the two HFI high-end frequencies to be better than 3%. Relative calibration based on diffuse foreground component separation gives consistent numbers (see table 6 of Planck Collaboration X 2016). Compared to 2013, calibration factors changed by 1.9 and 4.1% at 545 and 857 GHz, respectively. Combined with other pipeline changes (such as the ADC corrections), the brightness of the released 2015 frequency maps has decreased by 1.8 and 3.3% compared to 2013.

5.4.3. Relative calibration and consistency

The relative calibration of LFI, HFI, and WMAP can be assessed on several angular scales. At $\ell = 1$, we can compare the amplitude and direction of the Solar dipole, as measured in the frequency maps of the three instruments. On smaller scales, we can compare the amplitude of the CMB fluctuations measured frequency by frequency by the three instruments, during and after component separation.

– *Comparison of independent measurements of the Solar dipole.* Table 1 gives the LFI and HFI measurements of the Solar dipole, showing agreement well within the uncertainties. The amplitudes agree within 1.2 μK (0.04%), and the directions agree within 4′. Table 1 also gives the "nominal" *Planck* dipole that has been subtracted from the *Planck* frequency maps in the 2015 release. This is a plausible combination of the LFI and HFI values, which satisfied the need for a dipole that could be subtracted uniformly across all *Planck* frequencies early in the data processing, before the final systematic uncertainties in the dipole measurements were available and a rigorous combination could be determined. See Planck Collaboration VIII (2016) Sect. 5.1 for additional measurements.

Nearly independent determinations of the Solar dipole can be extracted from individual frequency maps using component-separation methods relying on templates from low and high frequencies where foregrounds dominate (Planck Collaboration V 2016; Planck Collaboration VIII 2016). The amplitude and direction of these Solar dipole measurements can be compared with each other and with the statistical errors. This leads to relative gain calibration factors for the $\ell = 1$ mode of the maps expressed in K_{CMB} units, as shown for frequencies from 70 to 545 GHz in Table 4. For components of the signal with spectral distribution different from the CMB, a colour correction is needed to take into account the broad bands of these experiments.

– *Comparison of the residuals of the Solar dipole left in the CMB maps after removal of the best common estimate.* Another measurement of relative calibration is given by the residuals of the Solar dipole left in CMB maps after removing the best common estimate, i.e., the nominal *Planck* dipole. (See Sects. 4 and 5.4.1 for details about how the dipole and quadrupole are handled.) The residual dipole comes from two terms, as illustrated in Fig. 5, one associated with the error in direction, with an axis nearly orthogonal to the Solar dipole, and one associated with the error in amplitude aligned with the Solar dipole. Using the 857 GHz map as a dust template (extrapolated with optimized coefficients derived per patch of sky), we find residual dipoles dominated by errors orthogonal to the direction of the Solar dipole at 100 and 143 GHz, and residuals associated with calibration errors for the other frequencies. The relative residual amplitudes are given in Table 4. This shows that a minimization of the dipole residuals can and will be introduced in the HFI calibration pipeline for the final 2016 release.

– *Comparison of CMB anisotropies frequency by frequency during and after component separation.* Table 4 also shows the relative calibration between frequencies and detectors determined by `SMICA` (Planck Collaboration XV 2014; Planck Collaboration IX 2016) and `Commander` (Planck Collaboration IX 2016; Planck Collaboration X 2016), two of the map-based diffuse component-separation codes used by *Planck*. The calculation is over different multipole ranges for the two methods, so variation between the two could reflect uncertainties in transfer functions. Moreover, `Commander` uses different constraints in order to deal with the complexities and extra degrees of freedom involved in fitting foregrounds individually (see Planck Collaboration X 2016 for details), so we do not expect identical results with the two codes. Nevertheless, the agreement is excellent, at the 0.2% level between the first

Table 4. Intercalibration factors by frequency between LFI, HFI, and WMAP.

Frequency [GHz] (Detector)	Solar dipole [%] $\ell = 1$	CMB Anisotropy [%] Commander $25 \le \ell \le 100$	CMB Anisotropy [%] SMICA $50 \le \ell \le 500$
30	...	$-0.3^a \pm 0.1$	...
44	...	$0.3^a \pm 0.1$	...
70	0.04^a	$0.0^a \pm 0.1$	$0.21^a \pm 0.06$
100	0.03	0.09 ± 0.02	0.03 ± 0.02
143	0^b	$0;\ -0.1 \pm 0.1^c$	0^b
217	0.20	$0;\ 0.02 \pm 0.03^c$	0.28 ± 0.02
353	0.53	0.5 ± 0.1	0.73 ± 0.11
545	1.25	-1.0^d	1.09 ± 1.5
WMAP 23 (K)	...	0^b	...
WMAP 33 (Ka)	...	0.1 ± 0.1	...
WMAP 41 (Q)	...	0.1 ± 0.1	...
WMAP 61 (V)	...	0.2 ± 0.1	...
WMAP 94 (W)	−0.26	0.2 ± 0.1	0.28 ± 0.15

Notes. [(a)] LFI map rescaling factors that are incorporated in the beam transfer functions, as described in Planck Collaboration II (2016), have been applied. [(b)] Reference frequency; no intercalibration calculated. [(c)] For Commander at 143 GHz, detector set "ds1" was used as a reference (intercalibration factor = 0). The mean intercalibration factor for detectors ds2+5+6+7 was -0.1 ± 0.1. Similarly, at 217 GHz detector "1" was used as a reference (intercalibration factor = 0), and the mean intercalibration factor for detectors 2+3+4 was 0.02 ± 0.03. See table 6 in Planck Collaboration X (2016) for details. [(d)] For Commander, the effective recalibration of the 545 GHz channel measured in units of μK_{cmb} is the product of a multiplicative calibration factor and a unit conversion correction due to revised bandpass estimation. See Sect. 5.3 in Planck Collaboration X (2016) for details.

acoustic peak, intermediate ℓ, and dipole residuals, and with intercalibration offsets between frequencies within 0.3% of zero from 30 GHz to 217 GHz.

The following points highlight the remarkable internal consistency of the *Planck* calibration.

- The small Solar dipole residuals measured for the 100 and 143 GHz channels (<4 μK) are close to 90° away from the adopted *Planck* Solar dipole, reflecting in both cases a small 2.′8 shift in the measured direction of the dipole compared to the adopted dipole, but amplitudes (hence calibrations) within 0.1% of the adopted ("mean") value. The Commander and SMICA inter-comparisons below and on the first acoustic peak give a calibration difference between 100 and 143 GHz of ≤0.09%, confirming the very high calibration accuracy of these two channels.
- The amplitude of the Solar dipole measured by the 70 GHz channel shows a difference of 1 μK (0.03%) with respect to the best HFI Solar dipole amplitude.
- The 217, 353, and 545 GHz channels show dipole residuals aligned with the Solar dipole, which thus measure directly calibration errors with respect to 143 GHz of 0.2, 0.53, and 1.25%.
- The SMICA first peak intercalibration of 217 and 353 GHz with respect to 143 GHz shows similar intercalibration to the dipole residuals, with differences of 0.08 and 0.20%. In fact, Table 4 suggests that we can now achieve significantly better intercalibration of all CMB channels from 70 to 353 GHz.
- Comparison of the Solar dipole and first acoustic peak intercalibration factors for the 545 GHz channel gives a difference of only 0.16%. This shows that the 545 GHz channel could be calibrated using the first acoustic peak of the CMB instead of planets. Use of the planet model could then be limited to intercalibration between 545 and 857 GHz. The roughly 1% agreement between the planets and CMB absolute calibrations also shows that the current uncertainties in the absolute

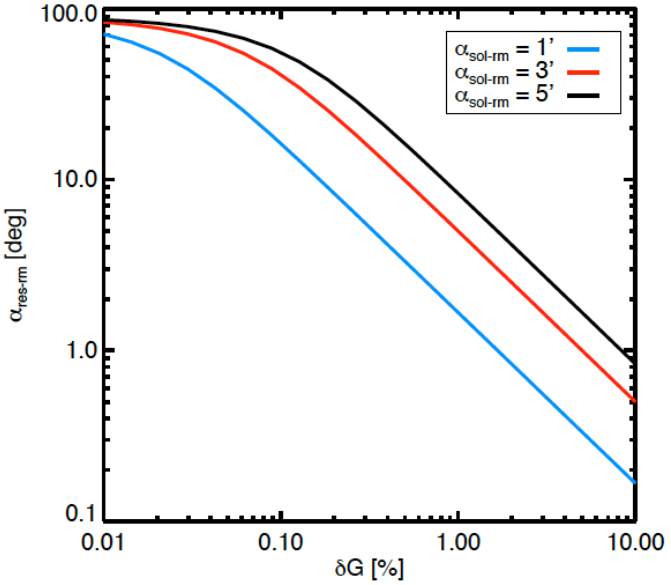

Fig. 5. Angle difference α_{res-rm} between the removed Solar dipole and the residual dipole for given errors on the dipole direction (i.e., the angle difference between the removed dipole and the true Solar dipole, α_{sol-rm}), and on the calibration ($\delta G = 1 - A_{rm}/A_{sol}$, expressed as a percentage).

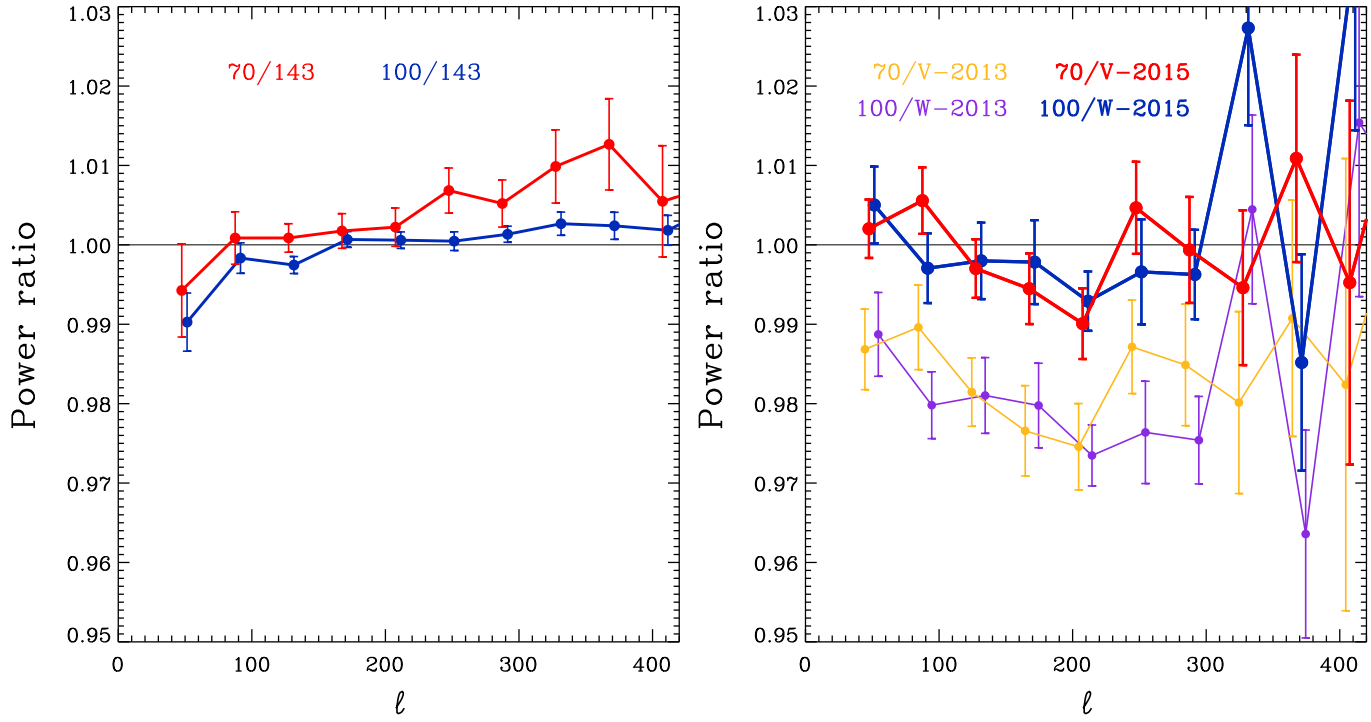

Fig. 6. Ratios of power spectra spanning the region of the first acoustic peak, uncorrected for foregrounds (which vary across the three frequencies), over 60% of the sky. The uncertainties are the errors in the mean within each $\Delta\ell = 40$ bin of the ratios computed ℓ by ℓ. *Left*: ratios of 70 and 100 GHz TT spectra to 143 GHz. The low values at $\ell = 50$ are due to diffuse foregrounds at 143 GHz. The rise to higher multipoles in the 70/143 ratio is due to discrete foregrounds. *Right*: ratio of TT spectra of *Planck* 70 and 100 GHz to WMAP V and W bands, as calculated for *Planck* 2013 data (Planck Collaboration XXXI 2014) and for the 2015 data. The near overlap of frequencies between the *Planck* and WMAP bands means that foregrounds have no appreciable effect on the ratios. The effect of the calibration changes in *Planck* between 2013 and 2015, which are discussed in this paper, is clear. There is now excellent agreement within statistical errors between *Planck* and WMAP in the region of the spectrum where both have high S/N.

calibration of the high-frequency channels, dominated by the roughly 5% error on the models, are probably overestimated.

– The intercalibration factors derived from `Commander` in all frequency bands from 70 GHz to 217 GHz are less than 0.1%. Considering all *Planck* bands from 30 GHz to 353 GHz, they are within 0.5%.

This comparison can also be made at the power spectrum level. The left-hand panel in Fig. 6 compares the 70, 100, and 143 GHz channels of LFI and HFI in the multipole range of the first acoustic peak, $50 < \ell < 500$, uncorrected for foregrounds, over 60% of the sky. The low values at $\ell = 50$ show the effect of unremoved diffuse foregrounds at 143 GHz, and the rise of the 70/143 ratio is at least partly driven by unremoved discrete foregrounds; the uncertainties are larger at 70 GHz as well. In the middle region, the agreement is very good, at a level of a few tenths of a percent. This result is a direct test that all systematic effects in calibration have been corrected on both instruments to better than this value.

The right-hand panel of Fig. 6 shows the ratios of *Planck* TT spectra at 70 and 100 GHz to those of WMAP in the V and W bands, as calculated for *Planck* 2013 data (Planck Collaboration XXXI 2014) and for the 2015 data. While the scatter is significantly larger than that in the left-hand panel, due to the higher noise in WMAP, the agreement is very good, and within the statistical errors. We can now say that within the uncertainties, LFI, HFI, and WMAP agree, and the difference seen in the 2013 data (Planck Collaboration XXXI 2014) is gone.

5.4.4. Summary of calibration

The *Planck* 70 and 100 GHz channels belong to instruments based on different technologies, with different systematic effects, and operating close to the minimum of the diffuse foregrounds. They thus provide a very good test of the consistency of calibration and transfer functions. The internal consistency between LFI and HFI is remarkable. Figure 6 represents a stringent test of calibration, systematic effects, beams, and transfer functions, and demonstrates overall consistency at a level of a few parts per thousand between independent instruments and spacecraft.

The *Planck* CMB-channels from 70 to 217 GHz show calibration differences below 0.3%, measured from both residual dipoles and the first acoustic peak. Using a Solar dipole reference established on the 100 and 143 GHz channels, it is likely that all detectors could be inter-calibrated to 0.05% in subsequent data processing versions. The agreement of the measured calibration factors from dipole residuals ($\ell = 1$) and the first acoustic peak ($\ell \approx 200$) shows that the transfer functions are controlled to better than 0.2% in this multipole range. Corrections for systematic effects in HFI cover a dynamic range from detector to detector larger than 2 at 100 and 143 GHz, but have reduced the calibration errors by an order of magnitude. This suggests that the corrections lead now to an absolute photometric calibration accuracy on the orbital dipole (limited only by systematics and noise) of 0.1%.

As in other instances in the *Planck* data processing, when very small systematic effects are detected and measured in a posteriori characterization, their removal from the data is complicated. Their determinations are often degenerate, and complete

Table 5. Main characteristics of LFI full mission maps.

Characteristic	Frequency band		
	30 GHz	44 GHz	70 GHz
Centre frequency [GHz]	28.4	44.1	70.4
Effective beam FWHM[a] [arcmin]	32.29	27.00	13.21
Effective beam ellipticity[a]	1.32	1.04	1.22
Temperature noise (1°)[b] [μK_{CMB}]	2.5	2.7	3.5
Polarization noise (Q and U; 1°)[b] [μK_{CMB}]	3.5	4.0	5.0
Overall calibration uncertainty[c] [%]	0.35	0.26	0.20
Systematic effects uncertainty in Stokes I^d [μK_{CMB}]	0.19	0.39	0.40
Systematic effects uncertainty in Stokes Q^d [μK_{CMB}]	0.20	0.23	0.45
Systematic effects uncertainty in Stokes U^d [μK_{CMB}]	0.40	0.45	0.44

Notes. [(a)] Calculated from the main beam solid angle of the effective beam, Ω_{eff} = mean(Ω). These values are used in the source extraction pipeline (Planck Collaboration XXVI 2016). [(b)] Noise rms computed after smoothing to 1°. [(c)] Sum of the error determined from the absolute and relative calibration, see Planck Collaboration IV (2016). [(d)] Estimated rms values over the full sky and after full mission integration. Not included here are gain reconstruction uncertainties, estimated to be of order 0.1%.

reprocessing is necessary. The calibration improvement demonstrated by the minimization of the dipole residuals using the 857 GHz dust template will be introduced in a self-consistent way in the HFI calibration pipeline and overall processing for the final 2016 release. Furthermore, the use of the Solar dipole parameters from the best *Planck* CMB channels (100 and 143 GHz) will be introduced in the processing of the channels more affected by foregrounds and noise. The LFI calibration accuracy is now close to noise-limited, but improvements will be made in 2016 according to a complete simulation plan to improve our understanding of calibration and systematics affecting low multipoles, particularly for polarization analysis.

6. Timelines

For the first time, the 2015 *Planck* release includes time series of the observations acquired by individual detectors in LFI and HFI (see Planck Collaboration II 2016 and Planck Collaboration VII 2016 for details). These timelines will be of use for those wishing to construct maps using specific time periods or mapmaking algorithms.

The delivered timelines have been cleaned of all major instrumental systematic effects. For LFI timelines, this cleaning means that the raw timelines are ADC-corrected, despiked, and demodulated; furthermore, the raw diode outputs (two per receiver) are combined and gain regularization is applied before calibration. For HFI timelines, this cleaning means that the raw timelines are ADC-corrected, demodulated, despiked, corrected for rare baseline jumps, and a dark template has been removed; they are converted to absorbed power units, and the time transfer function has been deconvolved.

The timelines are calibrated to astrophysical units and corrected for a zero-point value (determined at map level). The Solar and orbital dipole signals have been removed. In addition, for LFI, an estimation of Galactic stray light has been removed.

The timelines still contain the low-frequency noise that is later removed by destriping at the mapmaking stage. However, sets of offsets are provided (determined during mapmaking), which can be used to convert the calibrated timelines to maps without destriping. For LFI, the offsets are computed every 0.246, 0.988, and 1.000 s for the 30, 44, and 70 GHz channels, respectively, using the full mission data and all valid detectors per channel. These offsets are used to produce the full-mission LFI maps. For shorter period maps, different offsets are used that optimize noise cross-correlation effects; these are not delivered. For HFI, a single offset per ring is determined during mapmaking using the full mission data set and all valid detectors per channel. These offsets are then applied to all maps produced using any fraction of the mission (year, survey) or any subset of detectors (single detector, detector set).

The timelines are accompanied by flags that determine which data have been used for mapmaking, as well as pointing timelines, which are sampled at the same frequency as the data themselves.

7. Frequency maps

Figures 7 and 8 show the *Planck* 2015 maps. Note that *Planck* uses `HEALPix` (Górski et al. 2005) as its basic representation scheme for maps, with resolution labelled by the N_{side} value.

7.1. Mapmaking

7.1.1. LFI

Mapmaking takes as input the calibrated timelines, from which the cosmological and orbital dipole signals have been removed. An estimate of Galactic stray light is subtracted from the timelines prior to mapmaking, since this is difficult to correct at map level. As for the 2013 release, the LFI maps are produced using the `Madam` destriping code (Keihänen et al. 2010), enhanced with a noise prior, which enables accurate removal of correlated $1/f$ noise, while simultaneously minimizing systematic errors by judicious use of masks. The production of maps and covariance matrices is validated using the FFP8 simulations. The output of the code consists of sky maps of temperature and Stokes Q and U polarization, and a statistical description of residual noise in the maps in the form of pixel-pixel noise covariance matrices. These matrices are produced at N_{side} = 64. In addition to full-mission maps at both high and low resolution (N_{side} = 16), many other types of maps are produced, including those from single horns, single radiometers, single surveys, odd and even surveys, single years, and halves of the mission. The LFI maps are not corrected for beam shape, so that point sources in the map have